Hindawi
International Journal of Antennas and Propagation
Volume 2022, Article ID 1233714, 15 pages
https://doi.org/10.1155/2022/1233714

Research Article

Applying Polarimetric Target Decomposition to 2D Turntable ISAR Imagery of a Complex Vehicle

Sevket Demirci

Department of Electrical-Electronics Engineering, Mersin University, Ciftlikkoy 33343, Mersin, Turkey

Correspondence should be addressed to Sevket Demirci; sdemirci@mersin.edu.tr

Received 19 January 2022; Revised 24 May 2022; Accepted 16 June 2022; Published 19 July 2022

Academic Editor: Raffaele Solimene

The capabilities of polarimetric target decomposition in SAR-based ATR applications are investigated by using 2D turntable ISAR imagery of a T-72 tank. To characterize target's anisotropic scattering properties, wide-angle case is considered through the employment of a distinct polarimetric analysis procedure based on angular averaging of the covariance matrix. The results of the application of the three types of coherent decomposition, that is, Pauli, Krogager, and Cameron decomposition, and one incoherent decomposition, that is, eigenvector/eigenvalue decomposition, are analyzed and compared in terms of the identification of the physical scattering mechanisms. The usefulness of the various secondary parameters, including orientation, symmetry, and entropy, is also discussed. It is found that Pauli and Krogager decomposition can be readily applied for quick discrimination between the odd- and even-bounce reflectors. For a more detailed description of scattering mechanisms, either the Cameron or eigenvector/eigenvalue decomposition can be employed since their classification images are shown to be mostly consistent with each other. The results demonstrate that the decomposition features can be effectively utilized in subsequent ATR processes.

1. Introduction

One important application of Synthetic Aperture Radar (SAR) imaging is the automatic target recognition (ATR) of stationary and moving vehicles on the ground. This task usually requires a training set of ground-truth images for a typical range of target and data collection parameters. In particular, wide-angle collections have recently received increasing attention owing to the need for high-resolution imagery [1–5]. However, target signatures show strong fluctuations as the aspect angle varies, and thus, a considerably large dataset should be gathered for a representative range of view angles. Such wide-angle data can be more feasibly acquired by means of turntable Inverse Synthetic Aperture Radar (ISAR) imaging techniques.

In this context, SAR/ISAR images of manmade targets have been conventionally analyzed in the amplitude domain and for single-polarization data in relation to the ATR process. This analysis, however, lacks the ability to give much information about the scattering mechanisms and thereby the target's structural components. Polarimetric diversity can be exploited to overcome this limitation. It is well known that polarimetric radars, in principle, can sense the target shape, orientation, and symmetric structures. The difficulty with this technique, however, is that interpretation is difficult due to a multitude of variables such as wavelength, viewing geometry, and target properties. This has motivated the development of a substantial number of systems and methods, which have proven especially the usefulness of polarimetric SAR (Pol-SAR) in various applications [6–8].

Specifically, the so-called target (or polarimetric scattering) decomposition remains the most promising method for retrieving targets' physical parameters [9, 10]. The objective of target decomposition theorems is to break down the total scattering into a combination of simpler (canonical) responses for an easier interpretation. They are mainly categorized into two: coherent decomposition and incoherent decomposition. The former is based on the decomposition of the scattering matrix $[S]$ and is well-suited to deterministic (manmade) scatterers. The latter, on the other hand, is based on the decomposition of the coherency matrix $[T]$ or the covariance matrix $[C]$ and is often employed to

describe the scattering behavior of distributed (natural) scatterers. Among the popular types of coherent decomposition are the Pauli decomposition, Krogager decomposition, Cameron decomposition, and Huynen–Euler decomposition [6]. As for the incoherent decomposition, it is further rendered into two classes: eigenvector/eigenvalue-based decomposition and model-based decomposition. Specifically, the eigenvector/eigenvalue-based decomposition has the capability of incorporating the entire range of scattering mechanisms, and the parameters, namely, entropy (H) and mean alpha ($\overline{\alpha}$) derived from this decomposition, can also be utilized within unsupervised classification algorithms, like the well-known ($H/\overline{\alpha}$) classification. For a detailed discussion of target decomposition principles and applications, the reader is referred to [6, 9, 10].

In the literature, a few studies have dealt with polarimetric ISAR (Pol-ISAR) signatures of radar targets [11–26]. The progress in this area has been slow since the problem is difficult due to the high variation of scattering against the aspect angle. Also, the ground-truth data for a full-sized vehicle can be obtained either through cumbersome and expensive own measurements or from limited public sources. Consequently, there exists a few published examples, most of which employed anechoic chamber measurements of scale model targets. The usefulness of Cameron [16–18] and Pauli [19, 20] decomposition was tested on various targets, including simple reflectors, SLICY, car, and models of a tank and UAV. In [21–23], the performance of the Pauli, Krogager, and Cameron decomposition was compared with each other again on chamber data. Simulation implementation may also be a good representative of a practical situation. As an example, in [24], the numerical data of an unmanned aerial vehicle (UAV) were used in conjunction with a fusion of coherent decomposition. In [25, 26], the turntable ISAR data of a T-72 tank target [27] were analyzed via Pauli decomposition.

The aim of this study is to investigate the polarimetric scattering features of a complex vehicle for wide-angle SAR ATR applications. Specifically, the validity of polarimetric target decomposition is tested on X-band 2D turntable ISAR image data of a T-72 tank. To characterize wide-angle polarimetric signatures, a procedure based on angular averaging of the covariance matrices of subaperture images is proposed. Despite the challenges in the interpretation of structural characteristics from 2D signatures, the results of the application of the Pauli, Krogager, Cameron, and eigenvector/eigenvalue decomposition are analyzed and compared to infer the target's physical scattering mechanisms and features. The remainder of the paper is organized as follows. Methodology for the analysis of wide-angle polarimetric signatures is introduced in Section 3 after giving a brief theory of polarimetric ISAR and target decomposition in Section 2. The dataset description and the results are provided in Sections 4 and 5, respectively. Section 6 concludes the paper.

2. Theory

2.1. Polarimetric ISAR. Figure 1 shows the 2D monostatic turntable (circular) ISAR imaging geometry. The transceiver

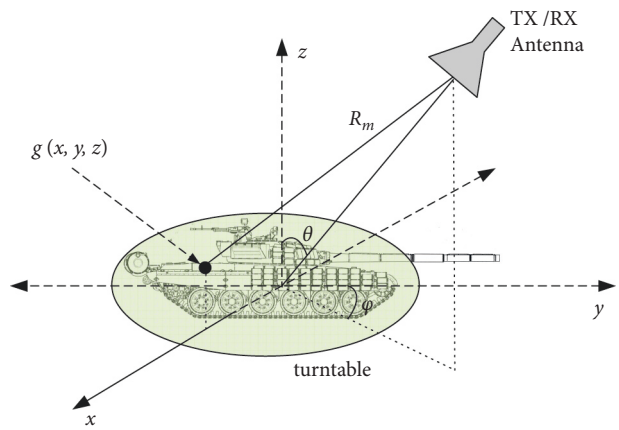

Figure 1: 2D monostatic turntable ISAR imaging geometry.

(TX/RX) antenna located at a fixed height illuminates the target placed on a turntable with a fixed incidence angle θ. The backscattering response is measured, step by step, at the uniform samples of azimuth (aspect) angle $\varnothing$, via rotating the target typically over a wide angular span. The echo signal for a single polarization and look-angle (θ, ϕ) can be expressed as

$$E_{\theta,\phi}(k_r) = \iint \int_{-\infty}^{\infty} g(x, y, z) \exp(-jk_r R_m) \mathrm{d}x \mathrm{d}y \mathrm{d}z, \quad (1)$$

where $g(x, y, z)$ is the reflectivity, k_r is the two-way radial wavenumber, and R_m is the distance from the antenna to the scatterers. The received 2D data matrix is then reconstructed to an image representing the projection of $g(x, y, z)$ onto the range-cross-range plane. To achieve an alias-free focused image, the imaging algorithm should compensate for the wavefront curvature effects resulting from such wide-angle observations. One option could be the spherical back-projection algorithm, a detailed formulation of which can be found in [28].

Linearly polarized (LP) radars measure the responses of the observed target with horizontal (H) and vertical (V) wave polarization, which are expressed in a scattering matrix

$$\left[S^{LP}\right] = \begin{bmatrix} S_{HH} & S_{HV} \\ S_{VH} & S_{VV} \end{bmatrix}, \quad (2)$$

where the elements S_{XY} are the complex scattering amplitudes for the transmit X and receive Y polarization. Each pixel retains these four elements, that is, two copolar S_{HH} and S_{VV} and two cross-polar S_{HV} and S_{VH}, which describe the amplitude and phase changes of the incident wave when scattered into the received polarization. Note that much of the information is contained in the amplitude ratios and relative phases of these elements; hence a precise external calibration procedure is usually required. Besides this disadvantage, polarimetric systems have the unique advantage that the information content of $[S]$ is independent of what polarization basis is used in its measurement. For example, circularly polarized (CP) backscattering can be generated from $[S^{LP}]$ through the transformation

$$\left[S^{CP}\right] = \begin{bmatrix} S_{RR} & S_{RL} \\ S_{LR} & S_{LL} \end{bmatrix} = \frac{1}{2}\begin{bmatrix} 1 & j \\ 1 & -j \end{bmatrix}\begin{bmatrix} S_{HH} & S_{HV} \\ S_{VH} & S_{VV} \end{bmatrix}\begin{bmatrix} 1 & 1 \\ j & -j \end{bmatrix}, \tag{3}$$

where subscripts L and R denote left-handed and right-handed circular polarization, respectively. It is also worth noting that all the analysis of this study will be given for monostatic measurements, for which $[S]$ becomes symmetric, that is, $(S_{XY} = S_{YX})$.

2.2. Polarimetric Target Decomposition. The main focus of this study is on the coherent decomposition wherein the scattering matrix $[S]$ is represented as a linear combination of elementary scattering mechanisms such as trihedral, dihedral, dipole, and helix. Trihedral or sphere-like scattering is characterized by an odd number of reflections and is insensitive to Line-of-Sight (LOS) rotations. Dihedral or diplane-like scattering corresponds to an even number of reflections and is extremely sensitive to the target's orientation angle ψ. Dipole-like scattering generally caused by wire-shaped targets is also dependent on the target orientation. Finally, helices always generate circular polarization regardless of the incident polarization. This type of scattering can be regarded as being composed of a double reflection mechanism of two dihedrals in a specific geometrical configuration. Herein, three most representatives of coherent decomposition as well as one incoherent example are considered, which are briefly reviewed in the following.

2.2.1. Pauli Decomposition. This decomposition in *LP* basis is given as

$$\left[S^{LP}\right] = \begin{bmatrix} S_{HH} & S_{HV} \\ S_{HV} & S_{VV} \end{bmatrix} = k_1[S]_s + k_2[S]_{d(0^\circ)} + k_3[S]_{d(45^\circ)}, \tag{4}$$

where

$$\left\{[S]_s, [S]_{d(0^\circ)}, [S]_{d(45^\circ)}\right\} = \left\{\frac{1}{\sqrt{2}}\begin{bmatrix} 1 & 0 \\ 0 & 1 \end{bmatrix}, \frac{1}{\sqrt{2}}\begin{bmatrix} 1 & 0 \\ 0 & -1 \end{bmatrix}, \frac{1}{\sqrt{2}}\begin{bmatrix} 0 & 1 \\ 1 & 0 \end{bmatrix}\right\}, \tag{5}$$

are the basis matrices and

$$k_1 = \frac{S_{HH} + S_{VV}}{\sqrt{2}}, \quad k_2 = \frac{S_{HH} - S_{VV}}{\sqrt{2}}, \quad k_3 = \sqrt{2}S_{HV} \tag{6}$$

are the complex coefficients. The first basis matrix denotes single or odd-bounce scattering from spheres, flat/curved surfaces, and trihedral corner reflectors (TCRs). The second matrix represents double- or even-bounce scattering caused by unrotated diplane structures such as from corners with a relative orientation angle of $\psi = 0^\circ$ with respect to the LOS. The last matrix corresponds to the scattering matrix of a dihedral rotated 45° about the LOS and thus indicates a loss of symmetry in $[S^{LP}]$. Hence, the weights k_1, k_2, and k_3 represent, respectively, the number of contributions of odd-bounce, diplane 0°, and 45° tilted diplane scatterings in the total $[S^{LP}]$. Pauli RGB image displays this information by assigning blue, red, and green colors to the magnitudes of $|k_1|$, $|k_2|$, and $|k_3|$, respectively.

The advantage of Pauli decomposition is that the three scattering components form an orthogonal set, and thus, they can be effectively utilized in further incoherent processing of distributed targets. On the other hand, the decomposition has the practical disadvantage that the last two components (i.e., unrotated and 45° tilted diplane) depend on the orientation of the scatterer. Thus, they effectively represent double-bounce scattering which makes the interpretation somewhat ambiguous.

2.2.2. Krogager Decomposition. In this approach, also called SDH decomposition, the scattering matrix is factorized into three elementary single scatterers: sphere, diplane, and helix. Since the helix is an uncommon scatterer, the decomposition is particularly suited for the determination of odd- and even-bounce scatterings. It can be more conveniently expressed on a CP basis as [6]

$$\left[S^{CP}\right] = \begin{bmatrix} S_{RR} & S_{RL} \\ S_{LR} & S_{LL} \end{bmatrix} = e^{j\varphi}\left\{e^{j\varphi_s}k_s[S]_s + k_d[S]_{d(\psi)} + k_h[S]_{h(\psi)}\right\}, \tag{7}$$

where

$$\left\{[S]_s, [S]_{d(\psi)}, [S]_{h(\psi)}\right\} = \left\{\frac{1}{\sqrt{2}}\begin{bmatrix} 0 & j \\ j & 0 \end{bmatrix}, \frac{1}{\sqrt{2}}\begin{bmatrix} e^{j2\psi} & 0 \\ 0 & -e^{-j2\psi} \end{bmatrix}, \frac{1}{2}\begin{bmatrix} e^{j2\psi} & 0 \\ 0 & 0 \end{bmatrix}\right\} \tag{8}$$

represent the scattering matrices for a sphere, diplane at angle ψ, and helix at angle ψ, on a CP basis, respectively, and

$$k_s = |S_{RL}|, \quad k_d = \min\left(|S_{RR}|, |S_{LL}|\right), \quad k_h = \operatorname{abs}\left(|S_{RR}| - |S_{LL}|\right), \tag{9}$$

are the corresponding weights. Moreover, φ is the absolute irrelevant phase term that depends on the distance between the radar and the target under study, and the phase φ_s is the displacement of the sphere to dihedral and helix components.

The distinctive property of this orientation invariant decomposition is that each of the three scattering

mechanisms can only appear in one out of three components, even though the diplane and helix matrices are not independent. This means that if two or more even-bounce scatterers exist within the same resolution cell, they can show up in diplane or helix components. However, noting that helix scattering is mostly generated by two or more dihedrals, a pure even-bounce scatterer can be uniquely distinguished by the absence of helix scattering.

2.2.3. Cameron Decomposition. For a reciprocal scattering that applies to monostatic radars, Cameron's approach is based on the symmetry properties of radar targets. A symmetric scattering in this regard is associated with targets having an axis of symmetry in the plane orthogonal to the LOS. Since targets have geometrically different symmetric features, discrimination can be first made by representing the measured matrix as the sum of two nonorthogonal components; that is, a largest or maximum symmetric scattering component $[S]_{\text{sym}}^{\max}$ and a minimum symmetric scattering component $[S]_{\text{sym}}^{\min}$ as

$$[S] = A\left[\cos\tau [S]_{\text{sym}}^{\max} + \sin\tau [S]_{\text{sym}}^{\min}\right], \tag{10}$$

where A is the amplitude (i.e., square root of the span) of $[S]$ and τ is the degree of symmetry of $[S]$. Helix-type scatterers can be distinguished at this stage since they have a minimal symmetric component. To identify other elementary symmetric scatterers, $[S]_{\text{sym}}^{\max}$ is further decomposed into a diagonal form through a rotation transformation. A complex parameter z extracted at this step is then used to classify the scatterer under consideration into one of the 6 common classes of symmetric scatterers: trihedral, cylinder, dipole, narrow diplane, dihedral, and quarter wave ($\lambda/4$). The approach involves both decomposition and classification steps and also returns a rotation angle parameter ψ_d, which is directly related to the orientation angle of the scatterer ψ by $= -\psi_d$. The approach's ability to both identify and orientate primitive scatterers permits a comprehensive analysis of radar targets. However, the inability to visualize the strength of individual scattering mechanisms can be stated as one drawback of Cameron's decomposition. Details about the expressions of the relevant parameters and classification scheme based on $[S]_{\text{sym}}^{\max}$ can be found in [6, 16].

2.2.4. Eigenvector/Eigenvalue Decomposition. In this incoherent decomposition, the coherency matrix $[T]$, formed from the outer product of the Pauli scattering vector $\vec{k}_P = 1/\sqrt{2}\,[S_{HH} + S_{VV}, S_{HH} - S_{VV}, 2S_{HV}]^T$, is written as

$$[T] = \sum_{i=1}^{3} \lambda_i \vec{e}_i \cdot \vec{e}_i^{+} = [T_1] + [T_2] + [T_3], \tag{11}$$

where λ_i are the eigenvalues, $\vec{e}_i$ are the eigenvectors, and the superscript + denotes conjugate transpose operation. Each of the $[T_i]$ matrices represents a single deterministic scattering process, the strength and type of which are determined by the corresponding eigenvalue and eigenvector, respectively. From these primary parameters, secondary parameters such as entropy H and mean alpha angle $\overline{\alpha}$ can be extracted. Entropy H represents the degree of randomness of scattering, and an entropy of 0 describes a nondepolarizing scattering, while an entropy value of 1 represents a fully depolarizing scattering. The mean alpha angle $\overline{\alpha}$ can be used to identify the underlying average scattering mechanism. It is a continuous parameter ranging from 0° to 90°; in general, $0^\circ \le \overline{\alpha} \le 30^\circ$, $40^\circ \le \overline{\alpha} \le 50^\circ$, and $60^\circ \le \overline{\alpha} \le 90^\circ$ correspond to surface, dipole, and dihedral scatterings, respectively. These two derived parameters can be used in pairs for classification purposes. The $H/\overline{\alpha}$ classification scheme is based on the division of the $H/\overline{\alpha}$ plane into 9 scattering classes (8 useable), as illustrated in [6].

3. Methodology for the Analysis of Wide-Angle Polarimetric Signatures

Manmade targets exhibit a stable scattering behavior in space and time and thus are termed coherent (deterministic) targets. A first-order descriptor such as the $[S]$ matrix can be directly used to describe such targets. Their signatures, however, show high variation with aspect angle ϕ and polarization. To investigate polarimetrically stable target areas over a certain range of ϕ, an averaged second-order polarimetric descriptor can be introduced. In this case, angular averaging is more appropriate than the conventional spatial averaging (i.e., multilook) since the returns from manmade objects are often spatially inhomogeneous. Thus, for each image pixel, one may construct an average covariance matrix $<[C]>_\phi$ (or a coherency matrix $<[T]>_\phi$) as

$$\langle [C] \rangle_\phi = \begin{bmatrix} C_{11} & C_{12} & C_{13} \\ C_{12}^* & C_{22} & C_{23} \\ C_{13}^* & C_{23}^* & C_{33} \end{bmatrix} = \begin{bmatrix} \langle |S_{HH}|^2 \rangle_\phi & \sqrt{2}\,\langle S_{HH} S_{HV}^* \rangle_\phi & \langle S_{HH} S_{VV}^* \rangle_\phi \\ \sqrt{2}\,\langle S_{HV} S_{HH}^* \rangle_\phi & 2\langle |S_{HV}|^2 \rangle_\phi & \sqrt{2}\,\langle S_{HV} S_{VV}^* \rangle_\phi \\ \langle S_{VV} S_{HH}^* \rangle_\phi & \sqrt{2}\,\langle S_{VV} S_{HV}^* \rangle_\phi & \langle |S_{VV}|^2 \rangle_\phi \end{bmatrix}, \tag{12}$$

$$\langle [T] \rangle_\phi = \begin{bmatrix} \langle |S_{HH} + S_{VV}|^2 \rangle_\phi & \langle (S_{HH} + S_{VV})(S_{HH} - S_{VV})^* \rangle_\phi & 2\langle (S_{HH} + S_{VV}) S_{HV}^* \rangle_\phi \\ \langle (S_{HH} - S_{VV})(S_{HH} + S_{VV})^* \rangle_\phi & \langle |S_{HH} - S_{VV}|^2 \rangle_\phi & 2\langle (S_{HH} - S_{VV}) S_{HV}^* \rangle_\phi \\ 2\langle S_{HV} (S_{HH} + S_{VV})^* \rangle_\phi & 2\langle S_{HV} (S_{HH} - S_{VV})^* \rangle_\phi & 4\langle |S_{HV}|^2 \rangle_\phi \end{bmatrix}, \tag{13}$$

where $< >_{\phi}$ means angular averaging and the superscript $*$ indicates complex conjugation. A relative scattering matrix $[S]^{\text{rel}}$ can then be retrieved from these angularly averaged values as [6]

$$[S]^{\text{rel}} = \begin{bmatrix} \sqrt{C_{11}} & \sqrt{C_{22}/2}\, e^{-j\varphi_{12}} \\ \sqrt{C_{22}/2}\, e^{-j\varphi_{12}} & \sqrt{C_{33}}\, e^{-j\varphi_{13}} \end{bmatrix} = \begin{bmatrix} |S_{HH}| & |S_{HV}| e^{j(\varphi_{HV}-\varphi_{HH})} \\ |S_{HV}| e^{j(\varphi_{HV}-\varphi_{HH})} & |S_{VV}| e^{j(\varphi_{VV}-\varphi_{HH})} \end{bmatrix}, \tag{14}$$

which can be subsequently deployed in a decomposition task. In order to make such an analysis, the methodology illustrated in Figure 2 was adopted. First, a predetermined number of subaperture (i.e., narrow-angle) quad-Pol-ISAR images were constructed and rotated to 0° target boresight. The average covariance matrix $<[C]>_{\phi}$ and coherence matrix $<[T]>_{\phi}$ were then calculated by using the $[S]$ matrix elements of each rotated image (equations (12) and (13)) and setting the average cross-pol channel as $S_{XY} = 1/2\,(S_{HV} + S_{VH})$. Next, the relative scattering matrix $[S]^{\text{rel}}$ was estimated via equation (14) and then used in coherent decomposition. In the eigenvector/eigenvalue decomposition, on the other hand, $<[T]>_{\phi}$ was directly used since it is an incoherent decomposition. Finally, the scattering features were interpreted from the relevant images.

4. Dataset

The dataset used in this study is the Georgia Tech Research Institute (GTRI) 3D full polarimetric ISAR data for a T-72 tank and can be publicly accessed online via the Air Force Research Laboratory (AFRL) website [27]. The dataset was acquired using an outdoor turntable/tower platform and at X-band (9.27 GHz to 9.93 GHz) with 3 MHz steps. It covers a total of 29 folders, each of which corresponds to a full angular aperture (i.e., 360°) views of the target at a specific depression angle. For each depression angle, there exists 85 subaperture (i.e., narrow-angle) data acquired with 3.9° angular bandwidths and 0.05° steps.

In this study, 9 subaperture data with filenames "$f115YY6 \sim f115YY14$" were utilized for a representative analysis of multiaspect polarimetric scattering. The number 115 in the filename indicates a depression angle of 30° (i.e., $\theta = 60°$), and the letters YY denote one out of the 4 pairs of TX/RX polarization. The whole angular coverage of the selected 9 subaperture data is from 25.49° to 63.39°. Figure 3 shows the target photo and its highly realistic CAD model on which principal target structures that are expected to give strong returns at the chosen look-angle are labeled.

5. Results

5.1. Preprocessing and Imaging. Prior to decomposition, data preprocessing steps were applied to narrow-angle data. First, the technique in [29, 30] was utilized to suppress zero-Doppler clutter, which is an inherent characteristic of turntable collections. The mean values of narrow-angle data were calculated for each frequency bin and subtracted from the corresponding frequency data. Second, a Hanning windowing and a zero padding with a factor of 4 were applied in the frequency domain. ISAR images were then reconstructed by using a near-field backprojection imaging algorithm [28].

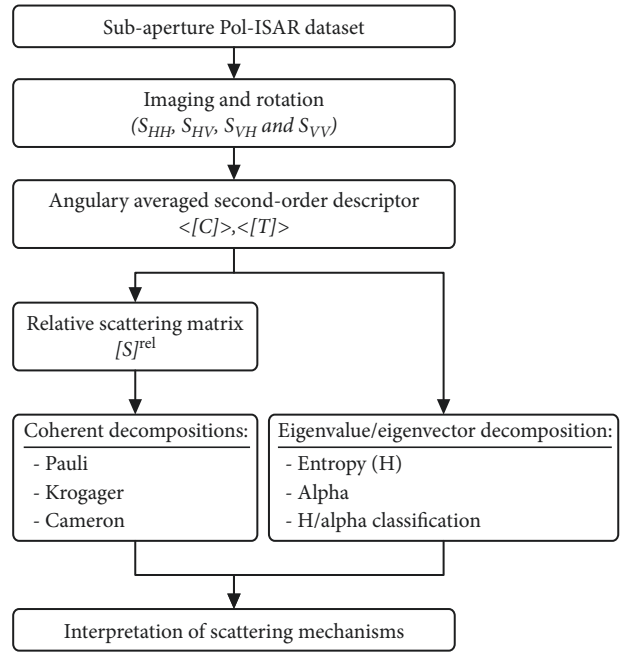

Figure 2: Methodological flow diagram of the polarimetric analyses used in this study.

Figure 4(a) shows $|S_{HH}|$ images for the corresponding angular section. The images for other channels are not presented for brevity. The right front, left-side, rear, and turret elements mostly produce strong backscattering at this aspect. The outline of the vehicle, the barrel, and the turntable platform can also be discerned from each image. However, the signatures, as expected, show considerable variation as the target pose changes. A more stable evaluation of this variation can be made on a CP basis. Figure 4(b), therefore, shows sample $|S_{RL}|$ images that are retrieved by applying the transformation in equation (3). The dominant scattering centers can be more easily identified through these orientation-independent signatures.

The relative scattering matrix $[S]^{\text{rel}}$ was then formed according to the procedure given in Figure 2. Figure 5 shows the amplitude images of the elements of this combined matrix. Scattering centers that are persistent over the azimuth span are enhanced because of angular averaging. Also, the HH response is seen to have higher magnitudes than those of other channels. Strong cross-pol scatterings are expected to belong to corner-like structures and complex parts such as wheels. The direct use of scattering matrix elements, however, is not able to provide much information about the scattering mechanisms. Hence, the above-mentioned decomposition theorems were applied to $[S]^{\text{rel}}$ whose results are given in the following.

5.2. Pauli and Krogager Decomposition. Figure 6 shows the Pauli decomposition results. In Figure 6(a), the three scattering components k_1, k_2, and k_3, which represent the

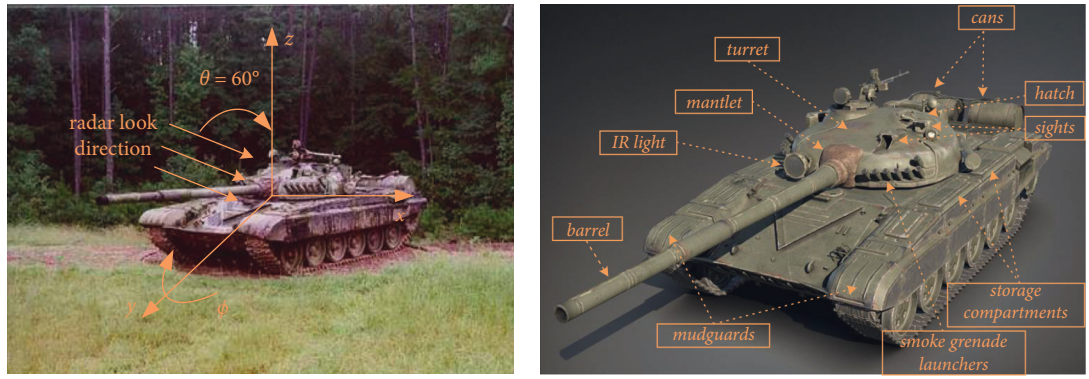

(a) (b)

FIGURE 3: T-72 tank. (a) Real target used in the experiment. (b) Highly accurate CAD model with names of some predominant target parts (photo by courtesy of Serhii Ryzhkov).

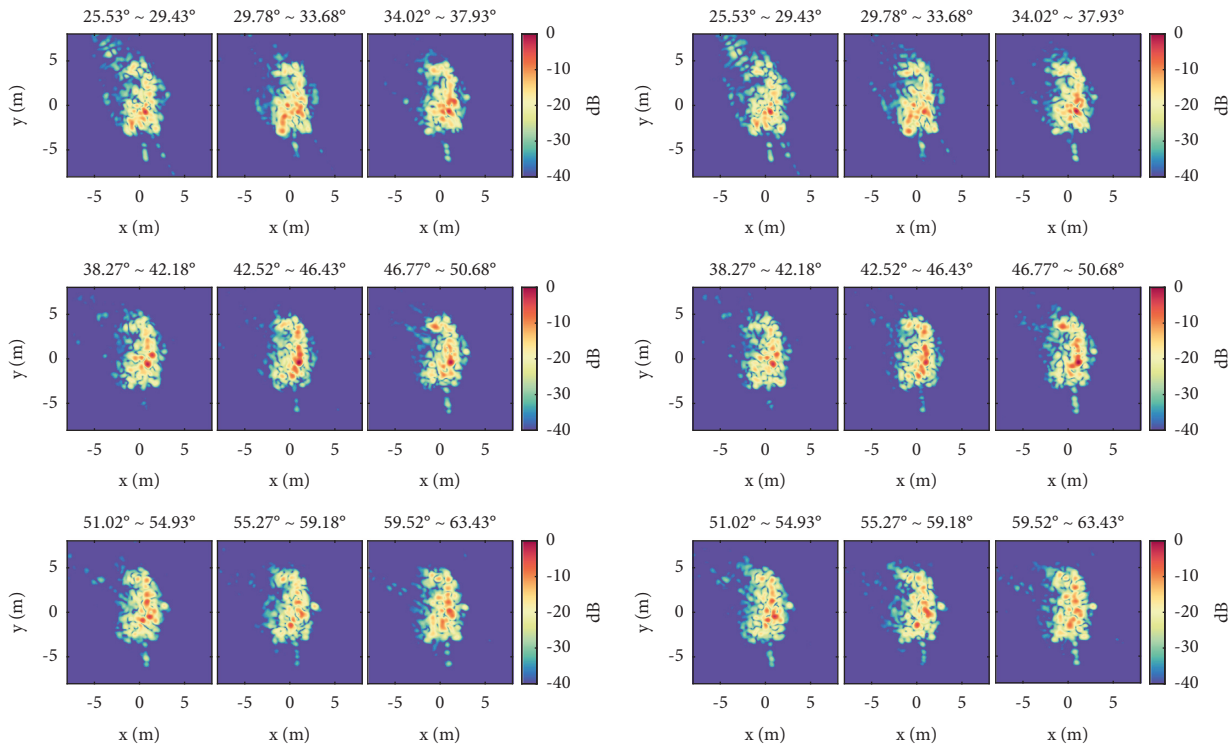

FIGURE 4: Changes in the (a)$|S_{HH}|$ and (b) synthetically generated $|S_{RL}|$ at 3.9° intervals over a range of 25.5° to 63.5° azimuth and 30° depression angle. The illumination is from the bottom at $x = 0$, and the target rotation is clockwise.

number of contributions of odd-bounce, even-bounce, and 45° tilted diplane scatterings, respectively, are displayed individually. A mixture of sphere (odd) and diplane 0° mechanisms is seen for the right front of the hull and left front of the turret. The rear part containing cans has also such mechanisms with higher intensities of even-bounce scattering. Relatively strong diplane 45° scattering belongs to the left side and right front of the hull. An artifact within the turntable platform can also be discerned in $|k_1|$ and $|k_2|$ images.

Figure 6(b) shows the Pauli RGB image with and without the CAD model. A wide color range results, making the interpretation somewhat difficult. Therefore, sample $[R; G; B]$ values giving, respectively, the contributions of $|k_1||k_1|$, $|k_2|$, and $|k_3|$ are also presented. The scattering mechanisms can be deduced by noting the proportion of $[R; G; B]$ values within the range $[0 - 255]$. Moreover, the image signatures are grouped into six regions, namely, C1 to C6, which match the target structures shown in the model photos. The following comments can be made by noting that the illumination direction is from the left-hand side of the target.

C1 is mainly composed of the wheel-track section and the dihedral structure formed by the right mudguard and

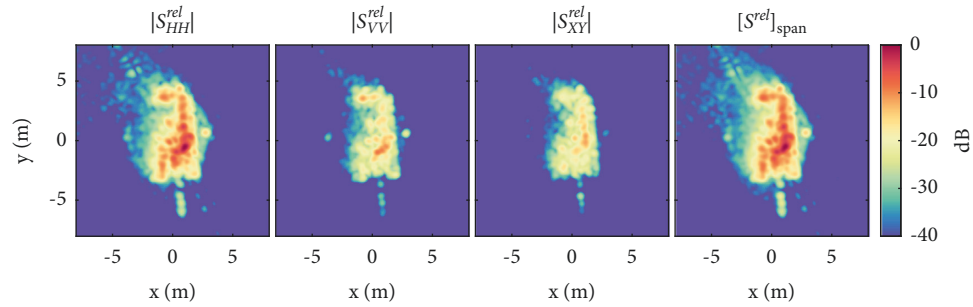

FIGURE 5: Amplitude and span images of the elements of $[S]^{rel}$ computed from the angularly averaged covariance matrix $<[C]>_{\phi}$.

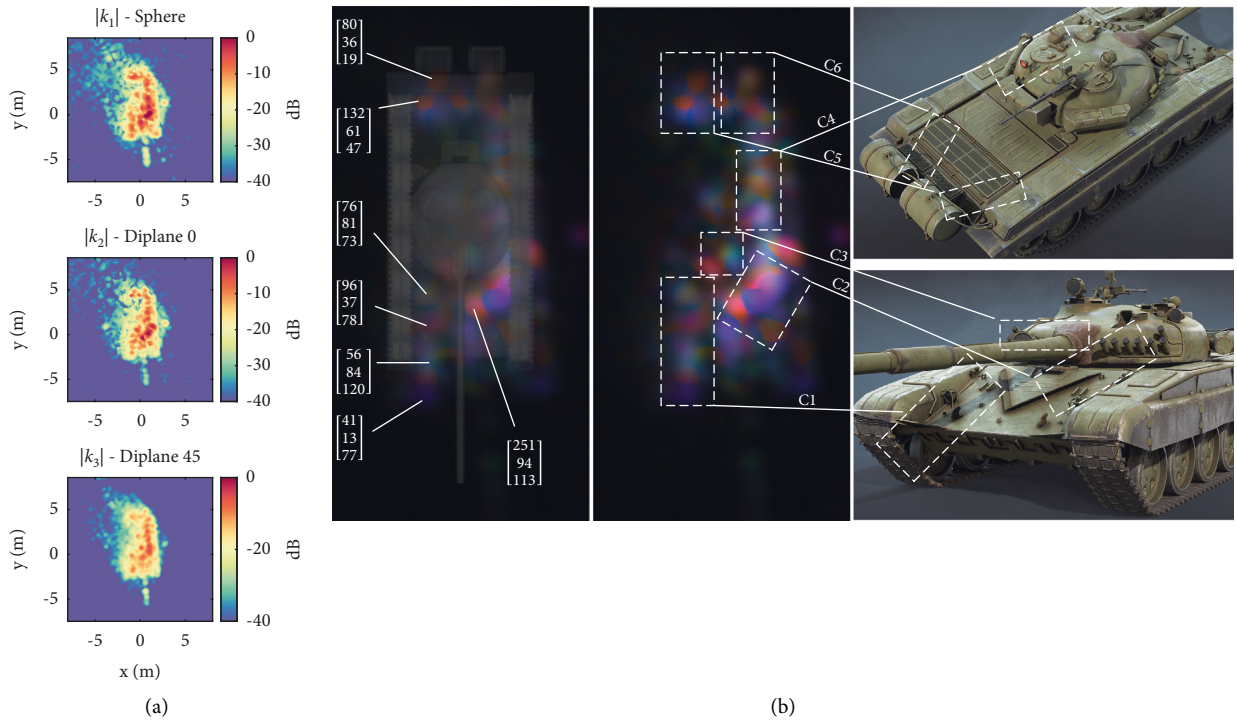

FIGURE 6: Pauli decomposition results. The three scattering components are displayed individually in (a) and as a composite RGB image in (b) with $R = |k_2|$, $G = |k_3|$, and $B = |k_1|$. Sample $[R; G; B]$ values and scattering regions C1 to C6 are also seen together with a 3D CAD model used for illustration purposes.

sloped front plate. There also exist several pieces, such as a driving light and a towing hook. These small objects and the dihedral structure are shown up in yellow, blue, and magenta tones in the upper part of C1. The lower part, on the other hand, includes the wheel-track section and has color tones varying from yellow to violet. The locations of these scattering mechanisms cannot be determined easily because of the complexity of the three-dimensional (3D) structure also involving the ground plane. C2 represents some portion of the V-shaped glacis plate, the smoke grenade launchers, and the joint between the turret ring and the hull. These parts and small objects stuck on the body give rise to dominant diplane 0° scattering in addition to secondary odd-bounce scattering. The bluish-violet tones are expected to be the odd bounces from the frontal plate. As for the C3 region, the left side of the mantlet behaves as a trihedral corner reflector (TCR), whereas the right side containing the IR light behaves as a diplane 0° reflector. The left side of the turret seen in C4 includes the two sight devices, hatch and snorkel tube. The radar signatures of this portion show relatively complicated scattering characteristics. Nevertheless, one sight equipment is seen to have magenta tones implying a coexistence of odd- and even-bounce mechanisms. C5 and C6 represent the signatures for the right and left rear of the vehicle, respectively. Cans and the structure around them are identified to have a dominant diplane 0° scattering mechanism.

Figure 7 shows the Krogager decomposition results. The amplitude images of the components k_s, k_d, and k_h are seen in Figure 7(a), while the composite RGB image and the CAD models are seen in Figure 7(b). Bluish colors are notably similar to that of the Pauli image, indicating the consistency of odd-bounce scattering features. Orientation invariant diplane scattering represented with red color also has fairly similar characteristics with Pauli's diplane 0° component.

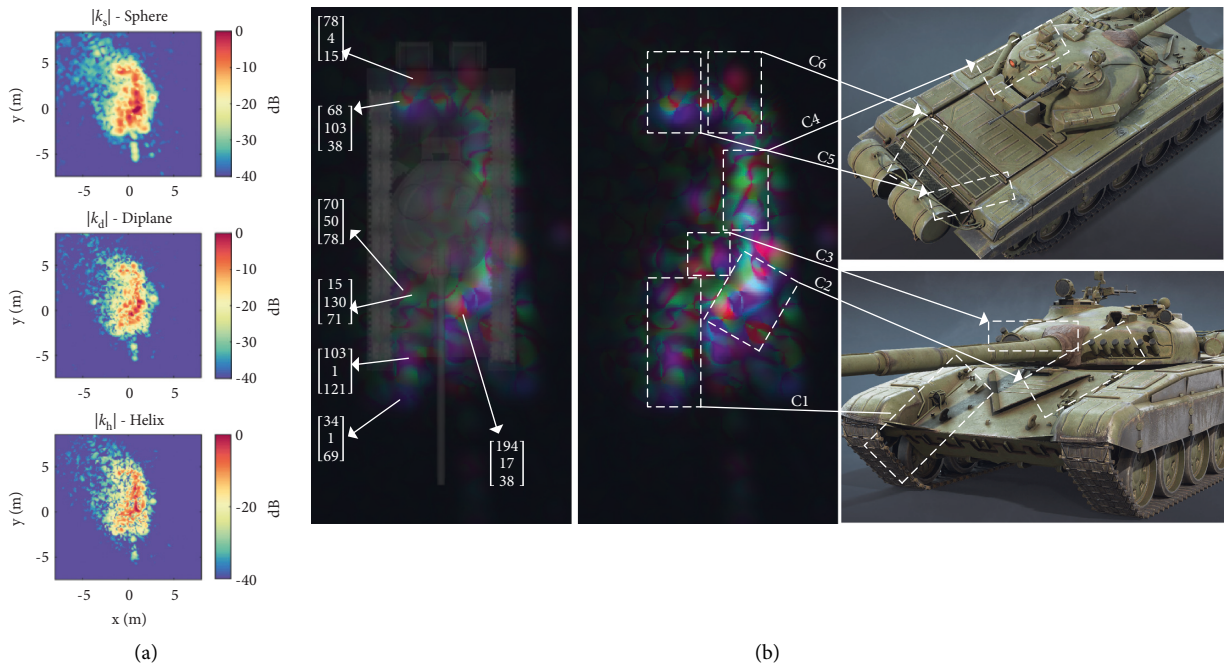

FIGURE 7: Krogager decomposition results. The three scattering components are displayed individually in (a) and as a composite RGB image in (b) with $R = |k_d|$, $G = |k_h|$, and $B = |k_s|$ image channels. Sample $[R; G; B]$ values and scattering regions C1 to C6 are also depicted together with a 3D CAD model used for illustration purposes.

Pure even-bounce mechanisms, in this case, however, can be more easily identified by figuring out the most reddish colors. Green color, on the other hand, represents helix scattering which can be attributed to the structures wherein two or more dihedrals exist within the same resolution cell.

To arrive at some further knowledge, a "winner takes all" classification scheme was applied. A target mask was first generated by applying a threshold to the span (i.e., total power) image in the dB scale. Then, the scattering mechanism with the highest coefficient is assigned to each pixel. The results for Pauli and Krogager decomposition are shown in Figure 8. For ready purposes, each of these types of coherent decomposition is shown to enable a quite appropriate identification of odd- and even-bounce mechanisms.

5.3. Cameron and Eigenvector/Eigenvalue Decomposition. To obtain a general idea of the performances of more advanced analyses, Cameron and eigenvector/eigenvalue decomposition were utilized. In all cases, a target mask calculated by thresholding the magnitudes of the total power image pixels in the dB scale was employed. Figure 9 presents the results for Cameron decomposition. The distribution of the three parameters extracted from this decomposition is shown in Figure 9(a), while their nominal values for the elementary mechanisms are given in Figure 9(b). To ease interpretation, their continuous values are classified into discrete subintervals with color coding. The angle τ is a measure of target symmetry and has a range $[0^\circ, 45^\circ]$. The resulting image reveals that most scatterers have low values of τ implying nearly symmetric scattering. Besides, some regions such as the left and right front, turret, and left rear exhibit asymmetric properties. Compared with Krogager's result, these asymmetric features match well the helix component, as expected. The distribution of the orientation angle ψ within the range $[-90^\circ, 90^\circ]$ is shown in the middle. Most regions fall into two classes $[-30^\circ - 0^\circ]$ and $[0^\circ - 30^\circ]$ with positive and negative signs indicate opposing orientations with respect to the radar. The last parameter is the classification parameter z which retains all scattering properties of symmetric scatterers. Its real part is shown in the bottom figure, from which sphere, cylinder/narrow-diplane, dipole, and diplane mechanisms can be identified by concerning the respective values given in Figure 9(b).

Figure 9(c) shows the classification image together with the class names and their color codes. Signatures shown in green do not differ very much from that of Krogager's helix component, thereby validating the accurate locating of asymmetric scatterers. As for the symmetric scatterers, we can observe from Figure 9(c) that almost all target regions are classified into one out of four scattering mechanisms, that is, cylinder, dipole, narrow-diplane, and $\lambda/4$ (quarter wave) device. The narrow-diplane mechanism can be thought of as a combination of diplane and dipole mechanisms. The layout of these signatures is highly similar to those of Krogager's diplane and Pauli's diplane 0° components. This can be readily seen when the images of the "winner takes all" scheme in Figure 8 are taken in comparison. Essentially, Cameron's image provides a more detailed identification of double-bounce scattering through discrimination between diplane and narrow-diplane mechanisms. The cylinder mechanism can be resulted from the blunt edges or from the surfaces which are strongly curved along one dimension. In the classification image, this

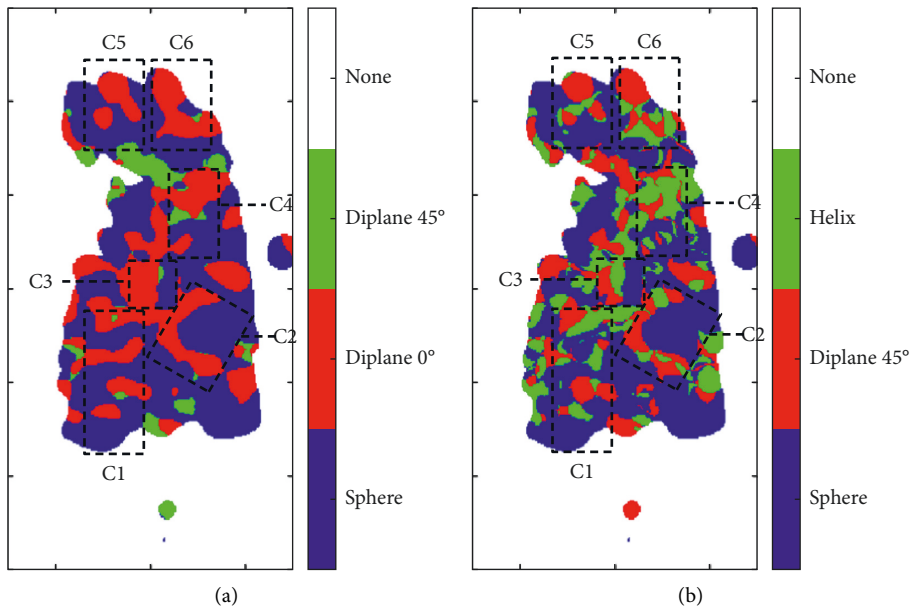

Figure 8: (a) Pauli and (b) Krogager decomposition results with a "winner takes all" classification scheme.

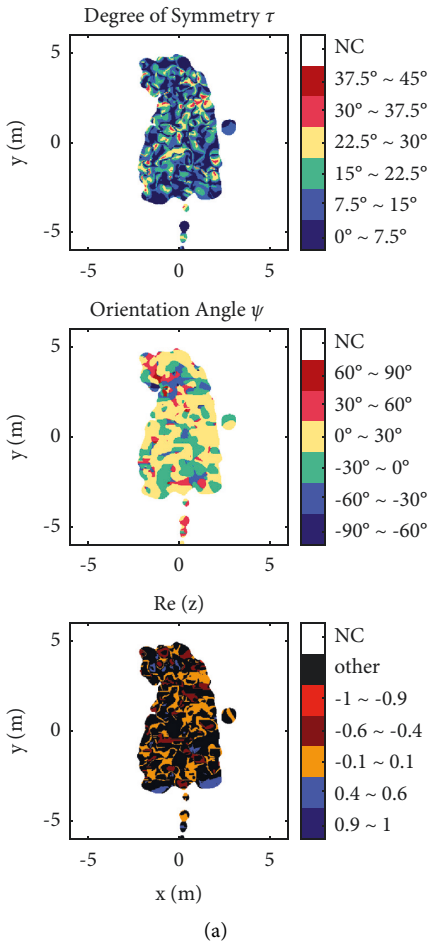

Scatterer		Cameron Parameter		
Symbol	Name	τ	ψ	z
$[S]_s$	Sphere, TCR	0	0	1
$[S]_{cyl}$	Cylinder	0	0	−1/2
$[S]_{dip\ (0°)}$	Dipole	0	0	0
$[S]_{dip\ (45°)}$	Dipole	0	45°	0
$[S]_{nd\ (0°)}$	Narrow Diplane	0	0	−1/2
$[S]_{d\ (0°)}$	Diplane	0	0	−1
$[S]_{\lambda/4(0°)}$	$\lambda/4$ Device	0	0	$\pm j$
$[S]_{hr/hl}$	Helix	45°	0	−1

(b)

Figure 9: Continued.

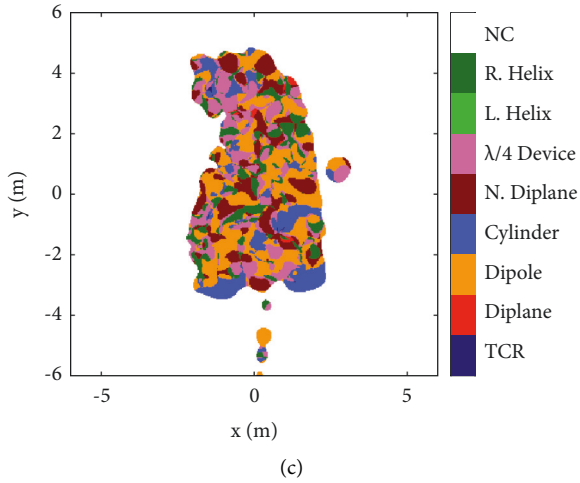

(c)

FIGURE 9: Cameron decomposition results. (a) Distributions of the three extracted parameters with (b) their nominal values for the elementary scatterers. (c) Classification image with classes and their color coding (NC: not classified).

is manifested most noticeably in the front regions of the tank as specular reflections. Note also that these regions are displayed as spheres/plates in both the Pauli and Krogager images (see Figure 8). This is due to the fact that the scattering matrix of a cylinder is composed of the sum of sphere/plate and dipole mechanisms, and Pauli and Krogager decomposition do not have the capability of resolving the dipole mechanism. In addition, most of the other sphere features in those images are displayed as dipole mechanism in Cameron's image. The main contributions of this scattering are presumably caused by edge diffractions from the surface body wherever discontinuities are present. It can also be caused by a superposition of double- and single-bounce mechanisms because the scattering matrix of a dipole can be regarded as the sum of these two mechanisms. Since the tank has so many discontinuities due to the components stuck all over its body, such a dominant dipole mechanism is likely to be expected. Lastly, the quarter-wave mechanism, which can be modelled as scattering from a specific configuration of the two dipoles, can be considered. The proportion of this mechanism is also seen to be large in the classified image. The target parts belonging to this mechanism cannot be derived easily but are expected to be the surface-dipole structures that are displaced from each other by a $\lambda/8$ distance.

The results for eigenvector/eigenvalue decomposition are given in Figure 10. The distributions of the three parameters, namely, mean alpha angle ($\overline{\alpha}$), entropy (H), and anisotropy (A), are plotted in Figure 10(a). The top figure shows the variation of $\overline{\alpha}$, which describes the average scattering mechanism. As being consistent with Cameron's result, most regions are classified as $30^\circ - 45^\circ$ and as $45^\circ - 60^\circ$, indicating the dominance of the dipole mechanism. Furthermore, the front corners and the cans at the rear section exhibit again anisotropic odd- and even-bounce reflections, respectively, with anisotropic means that $|S_{HH}| \neq |S_{VV}|$. The entropy H values of these two sections (see middle figure) are relatively low, implying a non-depolarizing (deterministic) scattering. The other parts possess moderate to high entropies owing to the presence of one or more secondary scattering mechanisms in addition to a dominant scattering mechanism. To characterize such random vector scatterings and provide complementary information to H, the anisotropy A is defined in the range from 0 to 1. In the cases of completely deterministic ($H = 1$) and completely depolarizing ($H = 0$) scattering processes, $A = 0$, and it gives no additional information. For moderate H values, a high value of A suggests that there exist only two important scattering processes, while a low value implies that the third scattering mechanism also plays a role. The bottom figure shows the variation of A for the investigated target. Since the target is dominated by relatively high A values and also moderate H values, only one secondary scattering mechanism can be estimated for the majority of the target.

Finally, the $H/\overline{\alpha}$ classification result is shown in Figure 10(c), while the scattering classes $Z1$ to $Z8$ and their color codes are depicted in Figure 10(b). The classes $Z6$, $Z7$, and $Z8$ indicate a dominant coherent backscattering whereas $Z3$, $Z4$, and $Z5$ indicate a moderately random backscattering with double-bounce, dipole, and odd-bounce mechanisms, respectively. On the whole, the image can be recognized to have nearly identical information to the previous results, especially with Cameron's one. In this case, however, the level of the randomness of odd-bounce, dipole, and double-bounce scattering is also manifested. For example, pure and multiple scattering types of a dominant even-bounce mechanism can be distinguished through pinpointing red and brown colors, respectively.

5.4. Analysis of Azimuthal Variation of Polarimetric Backscattering. In the previous section, the validity of the polarimetric decomposition and angular averaging based on multiaperture processing was investigated for a fixed number of subaperture images over 37.9° span. An important issue in such kind of processing is the targets' aspect-dependent scattering behavior resulting from their

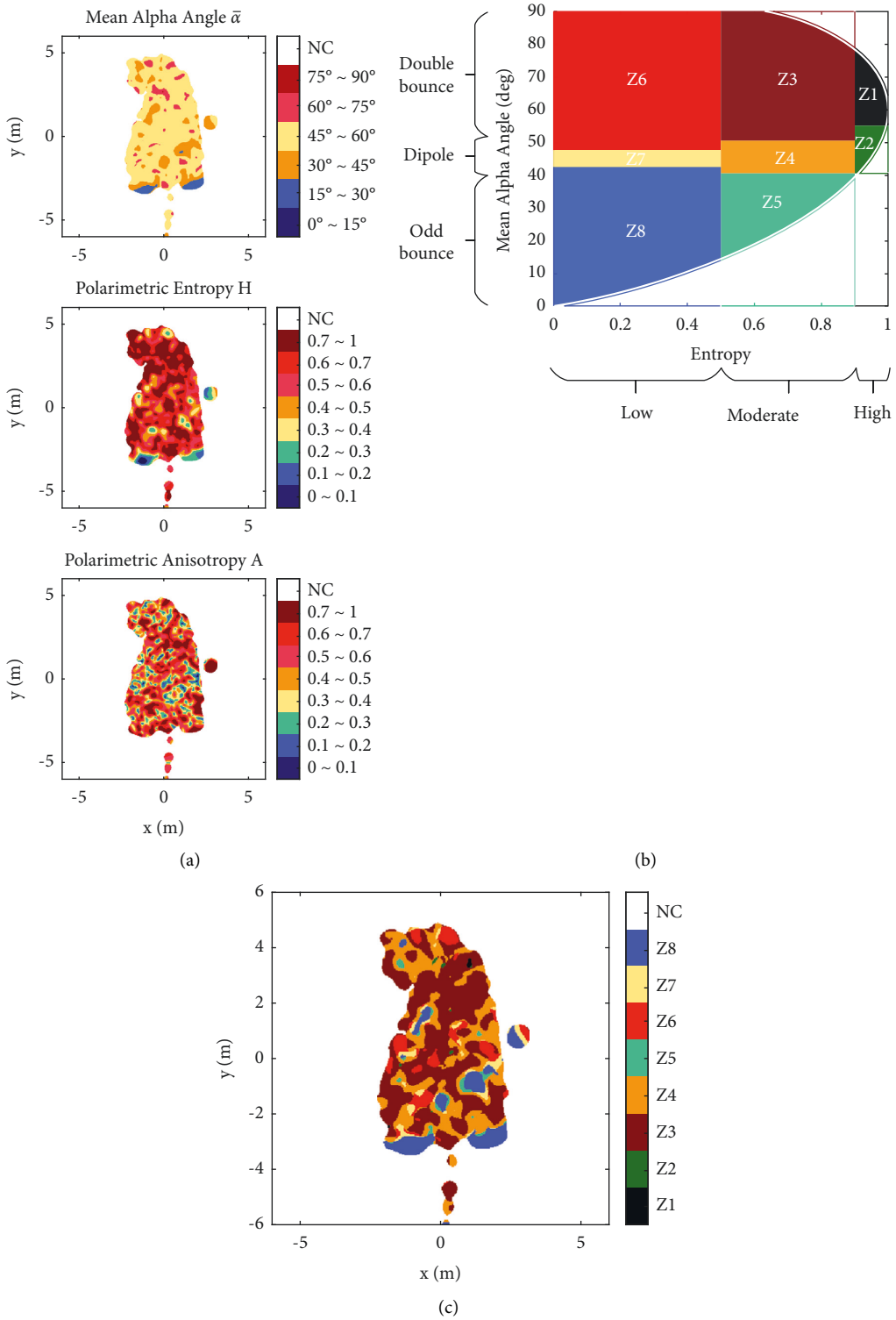

FIGURE 10: Eigenvector/eigenvalue decomposition results. (a) Distributions of the three extracted parameters. (b)$H/\bar{\alpha}$ classification plane with its division into eight classes and their color coding. (c)$H/\bar{\alpha}$ classification result (NC: not classified).

anisotropic geometric structures. These structures give rise to highly variant scattering characteristics as the aspect angle changes, which in turn affects the image intensities and polarimetric descriptors. For this reason, the angular, especially the azimuthal variation of polarimetric backscattering, should also be considered in relation to the effectiveness of the proposed scheme.

The image reconstruction of subaperture data is based on coherent integration of the responses of each scatterer for the corresponding subaperture bandwidth. Since angular

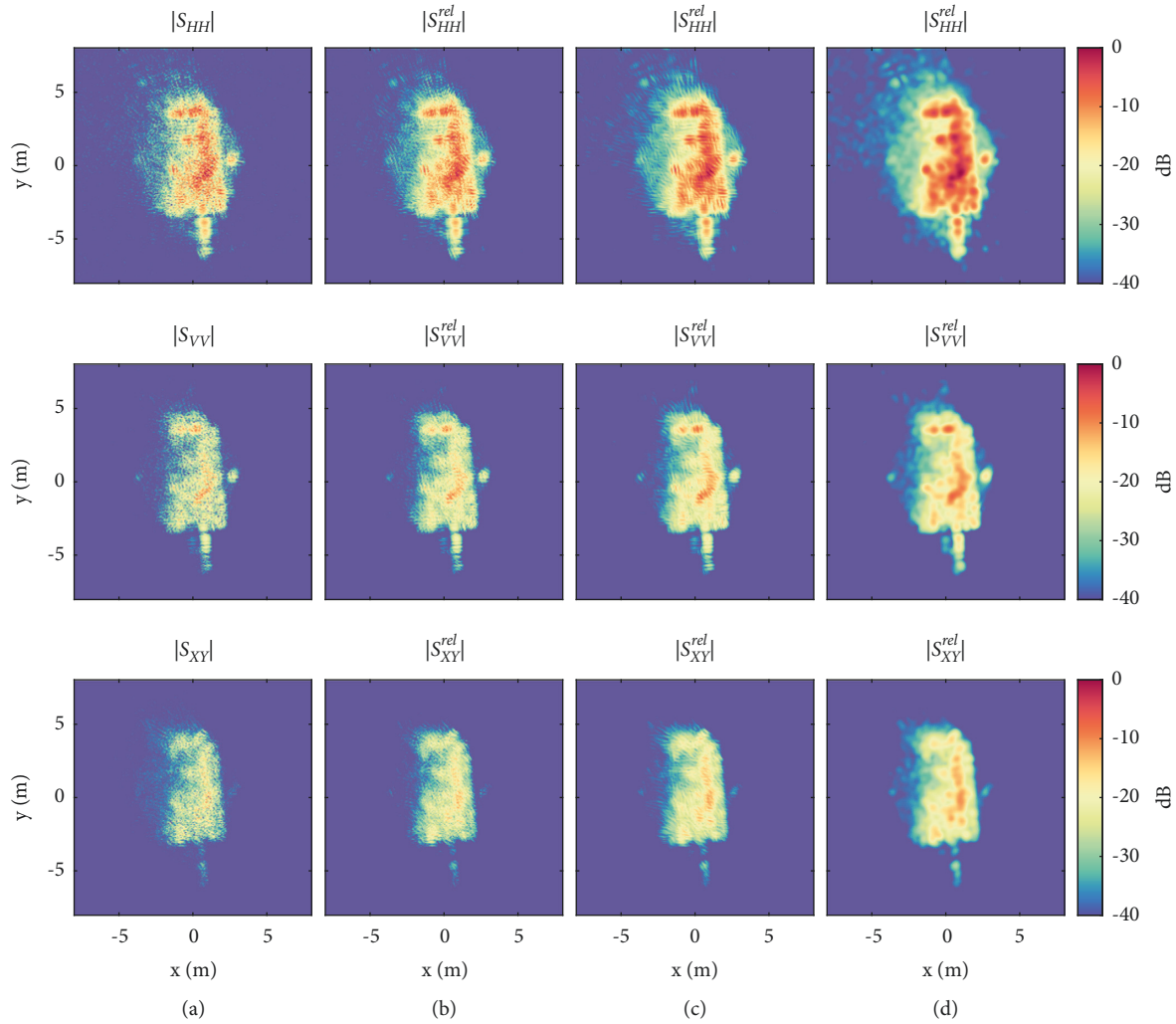

FIGURE 11: Scattering matrix elements for four different processing cases of $\Delta\phi = 88.9^{\circ}$ azimuth data. (a) Coherent imaging over the entire extent (case 1). Subaperture-based imaging with a subaperture number of (b) 3 (case 2), (c) 7 (case 3), and (d) 21 (case 4).

bandwidth determines image resolution, a smaller number of subdivisions should be employed when resolution is important. On the other hand, if the main objective is to preserve nonstationary scattering features, a large number of subapertures can be employed with the drawback of reduced image resolution. Hence, a trade-off has to be made concerning the degree of scattering description and the spatial resolution.

The current dataset covers the full-azimuth (360°) observation of the target. To get insight into the refined description of polarimetric backscattering under look-angle variation, different cases of azimuthal processing were considered for the 4.2° to 93.1° range. Case 1 corresponds to the coherent whole azimuth processing, whereas Cases 2, 3, and 4 correspond to the processing with a number of 3, 7, and 21 subapertures of which subaperture bandwidths are 29.4°, 12.4°, and 3.9°, respectively. Note that Case 4 matches the processing of the former section except with a different azimuth span and number of subapertures.

Figure 11 shows the amplitude images of the elements of the scattering matrices for the four cases. Resolution is highest for coherent processing and lowest for the largest number of subapertures, as expected. However, as the number of subapertures increases, the scatterers which do not have persistent scattering over the entire angular extent are better visualized within the same dynamic range.

The decomposition and entropy (H) images for the four cases are presented in Figure 12. Since Case 1 involves coherent integration of whole azimuth data without averaging, $H = 0$ values result, which represents completely deterministic scattering. Hence, the $H/\overline{\alpha}$ image for this case is not much meaningful to interpret.

First, a comparison between coherent and subaperture-based processing can be made. For this, consider the scattering mechanism features in Pauli, Krogager, and Cameron images of Figure 12 (a) and those of Figure 12 ((b) to (d)). A better visualization is accomplished in each case of subaperture processing mainly due to its low-resolution attribute. Also, the features, at first glance, seem to not vary so much and thus do not depend on whether the processing is coherent or subaperture-based. A detailed interpretation, however, can be done by comparing specific mechanisms.

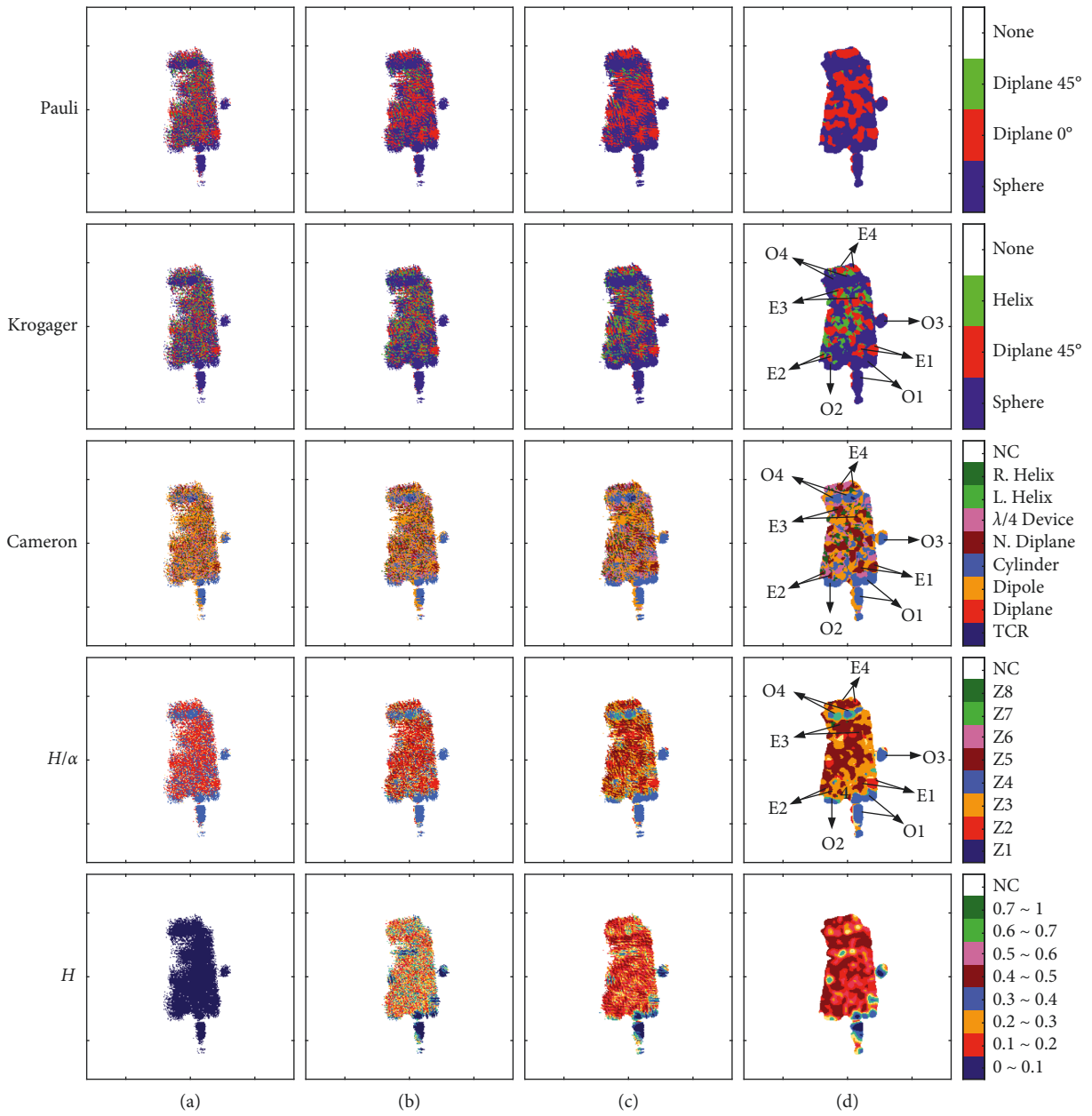

FIGURE 12: Polarimetric decomposition results for four different processing cases of $\Delta\phi = 88.9^{\circ}$ azimuth data. (a) Coherent imaging over the entire extent (case 1). Subaperture-based imaging with a subaperture number of (b) 3 (case 2), (c) 7 (case 3), and (d) 21 (case 4).

Note that the degree of consistency between decomposition results is maximum for Case 4 (see Figure 12 (d)), which has the largest number of subapertures. For this reason, four odd-bounce and four even-bounce mechanisms are selected from Case 4, which are labeled in Figure 12 (d) as O1 to O4 and E1 to E4, respectively. As an example, consider the Cameron results. All odd-bounce features are clearly displayed in each case of subaperture processing, whereas O2 (right front of the target) is hardly visible in coherent cases. As for even-bounce mechanisms, the Cameron result of Figure 12 (a) is lacking to provide apparent signatures of E3 and E4 at the rear section of the target. The same comments can be applied to the Krogager results. It can be concluded that odd-bounce features of the target belong to isotropic (or persistent) scatterers such as cylinders or curved surfaces as they exhibit stable scattering behavior over the wide azimuth span. Therefore, both processing types can be utilized for such targets. On the other hand, double- or even-bounce features show mostly anisotropic characteristic, which is manifested by the loss of polarimetric information in the coherent processing case.

Secondly, the effects of subaperture number can be evaluated. Let us consider first the variation of features of a specific decomposition. For instance, dipole scatterings in $H/\overline{\alpha}$ images show significant differences. Two scattering classes (red and blue) dominate the corresponding image of Case 2, whereas additional scattering classes exist in those of Cases 3 and 4. Therefore, as the subaperture number

increases, $H/\overline{\alpha}$ classification provides a more notable and detailed description of scattering mechanisms. The other types of decomposition, namely, Krogager and Cameron, are observed to be less sensitive to the subaperture number utilized. Next, let us examine the consistency of scattering features between decomposition approaches. In all three cases of subaperture processing, the labeled odd-bounce and even-bounce features are seen to be mostly invariant with the decomposition procedure. As for dipole scattering, a comparison between Cameron and $H/\overline{\alpha}$ can be made. It can be discerned that the spatial uniformity of this scattering between types of decomposition is high for Case 3 and Case 4, whereas it is very low for Case 2, wherein the lowest subaperture number is exploited. Thus, it can be concluded that the general agreement between types of decomposition decreases as the number of subapertures decreases. The overall considerations show that a subaperture bandwidth around 12° would be a satisfactory compromise between image quality and accurate characterization of polarimetric scattering.

6. Conclusions

The feasibility of using polarimetric target decomposition in wide-angle SAR/ISAR imaging-based ATR applications was evaluated by means of experimental ISAR data of a T-72 tank. For this purpose, multiaspect narrow-angle images were first reconstructed by a spherical backprojection imaging algorithm and then rotated to the same aspect. The covariance matrices of the rotated images were then calculated and combined into a single matrix $<[C]>_{\phi}$ through an angular averaging. The relative scattering matrix $[S]^{\text{rel}}$ was then retrieved from $<[C]>_{\phi}$ and imaged to identify the scattering centers persistent over the synthesized angular span. Finally, the total target scattering contained in $[S]^{\text{rel}}$ was expressed as a combination of elementary scattering processes via the application of coherent and incoherent decomposition algorithms.

Due to the complex target structure and its 2D representation, most target parts were observed to have a sophisticated scattering, as expected. Nevertheless, each algorithm is able to provide satisfactorily efficient means to interpret dominant scattering mechanisms. For quick discrimination between the odd- (sphere, flat surface, or TCR) and even-bounce (dihedral) reflectors, Pauli and Krogager decomposition can be utilized with a subsequent a "winner takes all" classification scheme. It should be noted, however, that in Pauli decomposition even-bounce reflectors appear in two components and interpretations can be somewhat misleading. As for the third scattering components, Pauli's 45° rotated diplane can be difficult to interpret, whereas Krogager's helix scattering can be useful in determining the asymmetric scatterers, which is also validated by Cameron's result.

Cameron and eigenvector/eigenvalue decomposition include more canonical scatterers, thereby providing a more detailed explanation of physical scattering mechanisms. In the eigenvalue/eigenvector decomposition, each of the three mechanisms, namely, the odd-bounce dipole and even-bounce mechanisms, is further separated into two classes to deduce the level of secondary scattering mechanisms given by entropy. On the other hand, the different scattering classes are used in Cameron decomposition to describe such complex scatterings. When compared in pairs, each classification image presents similar information for the investigated target; for example, as consistent with expectation, cylinder and dipole signatures in Cameron's result match well the low-entropy odd bounce (Z8) and medium entropy dipole-like (Z4) signatures, respectively. In general, the results demonstrate the usefulness of target decomposition in polarimetric SAR/ISAR-based ATR applications. However, the study can also be improved by means of 3D imaging and/or quantitative analyses of the classification results.

Data Availability

Data used are available at https://www.sdms.afrl.af.mil/index.php?collection=gtri.

Conflicts of Interest

The author declares no conflicts of interest.

References

[1] D. Feng, X. Pan, and G. Wang, "High-resolution ISAR imaging with wideband V-FM waveforms," *International Journal of Antennas and Propagation*, vol. 2017, Article ID 1908204, 10 pages, 2017.

[2] T. Feng and L. Guo, "Multiview ISAR imaging for complex targets based on improved SBR scattering model," *International Journal of Antennas and Propagation*, vol. 2021, Article ID 6615154, 10 pages, 2021.

[3] J. Feng, Y. Sun, and X. Ji, "High-resolution ISAR imaging based on improved sparse signal recovery algorithm," *Wireless Communications and Mobile Computing*, vol. 2021, Article ID 5541116, 7 pages, 2021.

[4] R. Hu, Z. Peng, and J. Ma, "A vehicle target recognition algorithm for wide-angle SAR based on joint feature set matching," *Electronics*, vol. 8, pp. 11–1252, 2019.

[5] F. Teng, Y. Lin, Y. Wang, W. Shen, S. Feng, and W. Hong, "An anisotropic scattering analysis method based on the statistical properties of multi-angular SAR images," *Remote Sensing*, vol. 12, p. 2152, 2020.

[6] J. Lee and E. Pottier, *Polarimetric Radar Imaging: From Basics to Applications*, Taylor & Francis, Abingdon, UK, 2009.

[7] J. van Zyl and Y. Kim, *Synthetic Aperture Radar Polarimetry*, John Wiley & Sons, Hoboken, NJ, USA, 2011.

[8] I. Hajnsek and Y. Desnos, *Polarimetric Synthetic Aperture Radar: Principles and Application*, Springer, Berlin, Germany, 2021.

[9] S. W. Chen, Y. Z. Li, X. S. Wang, S. P. Xiao, and M. Sato, "Modeling and interpretation of scattering mechanisms in polarimetric synthetic aperture radar: advances and perspectives," *IEEE Signal Processing Magazine*, vol. 31, no. 4, pp. 79–89, 2014.

[10] SW. Chen, XS. Wang, SP. Xiao, and M. Sato, "Advanced polarimetric target decomposition," in *Target Scattering Mechanism in Polarimetric Synthetic Aperture Radar,* Springer, Berlin, Germany, 2018.

[11] T. Heberling, D. Heberling, "Discrimination of scattering mechanisms via polarimetric rcs imaging [measurements

corner],” *IEEE Antennas and Propagation Magazine*, vol. 56, no. 3, pp. 154–165, 2014.

[12] S. Lischi, A. Lupidi, E. Martorella, and M. Martorella, “Enhanced ATR by jointly using Coherent and Incoherent Target Decomposition theorems on polarimetric ISAR images,” in *Proceedings of the 2014 11th European Radar Conference*, pp. 89–92, Rome, Italy, October 2014.

[13] D. hai, J.-ke Zhang, X.-song Wang, and S.-ping Xiao, “Superresolution polarimetric ISAR Imaging based on 2D CP-GTD model,” *Journal of Sensors*, vol. 2015, Article ID 293141, 11 pages, 2015.

[14] X. Y. Wang, T. Dallmann, R. Heberling, and D. Heberling, “ISAR Tomography for full-Polarimetric 3-D radar cross-section measurements,” *IEEE Transactions on Antennas and Propagation*, vol. 67, no. 4, pp. 2853–2858, 2019.

[15] Y. Yang, X.-S. Wang, Y.-Z. Shi, and L.-F. Shi, “RCS measurements and ISAR images of fixed-wing UAV for fully polarimetric radar,” in *Proceedings of the 2019 International Radar Conference (RADAR)*, pp. 1–5, Toulon, France, September 2019.

[16] W. L. Cameron, N. N. Leung, and L. K. Leung, “Simulated polarimetric signatures of primitive geometrical shapes,” *IEEE Transactions on Geoscience and Remote Sensing*, vol. 34, no. 3, pp. 793–803, 1996.

[17] L. I. Yongchen and Ya-Q. Jin, “Imaging and structural feature decomposition of a complex target using multi-aspect polarimetric scattering,” *Science China Information Sciences*, vol. 59, Article ID 082308, 2016.

[18] Q. Liu, C. Pang, Y. Li, and X. Wang, “Impact of polarization distortions on geometrical structure retrieval of moving man-made targets in ISAR Images,” *Electronics*, vol. 8, no. 4, p. 373, 2019.

[19] M. Martorella, A. Cacciamano, E. Giusti, F. Berizzi, B. Haywood, and B. Bates, “CLEAN technique for polarimetric ISAR,” *International Journal of Navigation and Observation*, vol. 2008, Article ID 325279, 12 pages, 2008.

[20] M. Martorella, E. Giusti, L. Demi et al., “Target recognition by means of polarimetric ISAR images,” *IEEE Transactions on Aerospace and Electronic Systems*, vol. 47, no. 1, 2011.

[21] M. Duquenoy, J. Ovarlez, L. Ferro-Famil, L. Vignaud, and E. Pottier, “Study of dispersive and anisotropic scatterers behavior in radar imaging using time frequency analysis and polarimetric coherent decomposition,” in *Proceedings of the IEEE Radar Conference*, pp. 180–185, Verona, NY, USA, April 2006.

[22] M. Duquenoy, J. Ovarlez, L. Ferro-Famil, E. Pottier, and L. Vignaud, “Scatterers characterisation in radar imaging using joint time-frequency analysis and polarimetric coherent decompositions,” *IET Radar, Sonar & Navigation*, vol. 4, no. 3, pp. 384–402, 2010.

[23] T. Dallmann, *Polarimetric Radar Cross-Section Imaging*, Aachen University, Ph.D. dissertation, 2017.

[24] H. Wu, B. Pang, D. Dai, J. Wu, and X. Wang, “Unmanned aerial vehicle recognition based on clustering by fast search and find of density peaks (CFSFDP) with polarimetric decomposition,” *Electronics*, vol. 7, no. 12, p. 364, 2018.

[25] S. Demirci, O. Ozdemir, and C. Ozdemir, “Interpretation and analysis of target scattering from fully-polarized ISAR images using Pauli decomposition scheme for target recognition,” *IEEE Access*, vol. 8, pp. 155926–155938, 2020.

[26] K. Xu and X. Xu, “A fast ISAR tomography technique for fully polarimetric 3-D Imaging of man-made targets,” *IEEE Transactions on Geoscience and Remote Sensing*, vol. 60, pp. 1–12, 2022.

[27] U. S. Air Force, “sensor data management system (SDMS),” 1997, https://www.sdms.afrl.af.mil/index.php?collection=gtri.

[28] S. Demirci, H. Cetinkaya, E. Yigit, and C. Vertiy, A. Vertiy, “A study on millimeter-wave imaging of concealed objects: application using back-projection algorithm,” *Progress In Electromagnetics Research*, vol. 128, pp. 457–477, 2012.

[29] J. D. Fowler, M. A. Temple, M. J. Havrilla, and J. J. Akerson, “Characterization of Zero-Doppler Clutter Removal Techniques for ISAR Applications,” in *Proceedings of the IEEE Radar Conference*, pp. 800–804, Waltham, MA, USA, April 2007.

[30] L. Zhang, Y. Zhang, “CSAR imaging with data extrapolation and approximate GLRT techniques,” *Progress In Electromagnetics Research M*, vol. 19, pp. 209–220, 2011.